https://doi.org/10.5194/acp-2021-1051
Preprint. Discussion started: 10 January 2022

Atmospheric Chemistry and Physics Discussions

Quantifying NO_x emissions in Egypt using TROPOMI observations

Anthony Rey-Pommier[1], Frédéric Chevallier[1], Philippe Ciais[1], Grégoire Broquet[1], Theodoros Christoudias[2], Jonilda Kushta[2], Didier Hauglustaine[1] and Jean Sciare[2].

[1] Laboratoire des Sciences du Climat et de l'Environnement, LSCE/IPSL, CEA-CNRS-UVSQ, Université Paris-Saclay, 91190 Gif-sur-Yvette, France
[2] The Cyprus Institute, Climate and Atmosphere Research Center, 2121 Nicosia, Cyprus

Correspondence: Anthony Rey-Pommier (anthony.rey-pommier@lsce.ipsl.fr)

Abstract. Urban areas and industrial facilities, which concentrate most human activity and industrial production, are major sources of air pollutants, with serious implications for human health and global climate. For most of these pollutants, emission inventories are often highly uncertain, especially in developing countries. Spaceborne observations from the TROPOMI instrument, onboard the Sentinel-5 Precursor satellite, are used to measure nitrogen dioxide (NO_2) slant column densities with a high spatial resolution. Here, we use two years of TROPOMI retrievals to map nitrogen oxides (NO_x = NO + NO_2) emissions in Egypt with a top-down model based on the continuity equation in steady state. Emissions are expressed as the sum of a transport term and a sink term representing the three-body reaction comprising NO_2 and OH. This sink term requires information on the lifetime of NO_2, which is calculated with the use of CAMS near-real-time temperature and hydroxyl radical (OH) concentration fields. The applicability of the OH concentration field is evaluated by comparing the lifetime it provides with the lifetime inferred from the fitting of NO_2 line density profiles with an exponentially modified Gaussian function. This comparison, which is conducted for 39 samples of NO_2 patterns above the city of Riyadh, provides information on the reliability of the CAMS near-real-time OH concentration fields; It also provides the location of the most appropriate vertical level to represent typical pollution sources in industrial areas and megacities in the Middle East. In Egypt, total derived emissions of NO_x are dominated by the sink term. However, they can be locally dominated by wind transport, especially along the Nile where human activities are concentrated. Megacities and industrial regions clearly appear as the largest sources of NO_x emissions in the country. Our top-down model produces emissions whose annual variability is consistent with the national electricity consumption. It is also able to detect lower emissions on Fridays, which are inherent to the social norm of the country, and to quantify the drop in emissions due to the COVID-19 pandemic. Overall, our indications of NO_x emissions for Egypt are found to be 25.0% higher than the CAMS-GLOB-ANT_v4.2 inventory, but significantly differ in terms of seasonality.

1 Introduction

Economic growth in developing countries has led to a strong increase of urban air pollution (Baklanov et al., 2016 [1]). Among the different pollutants, nitrogen oxides are key species. They are generally the products of fuel combustion, such as the combustion of hydrocarbons in the air at high temperature. The main sources of these compounds are therefore vehicle engines, but also heavy industrial facilities such as power plants, metal smelters and cement plants. Their accumulation in the lowest layers of the troposphere contributes to the formation of smog and acid rain (Singh et al., 2007 [2]). They also have a significant effect on human health, as they can cause various respiratory diseases (EPA, US., 2016 [3]). To deal with these phenomena, national and regional governments generally enact a series of air pollution control strategies, which typically take the form of bans on certain polluting technologies, with the aim of reducing the concentration of pollutants at the local level to targets that must be achieved within a given timeframe.

https://doi.org/10.5194/acp-2021-1051
Preprint. Discussion started: 10 January 2022

Atmospheric Chemistry and Physics Discussions

These strategies, which also help driving technological innovation, have had a significant effect in Europe (Crippa et al., 2016 [4]).

In Egypt, population growth, urbanisation, socio-economic development and the associated increase in the vehicle fleet led to a major degradation of air quality in the last decades, especially in highly populated areas such as Greater Cairo and the Nile Delta (Abou El-Magd et al., 2020 [5]), which gather the majority of the population. The Ministry of State for the Environment has thus initiated new policies that aim to reduce pollution levels throughout the country, through technical mitigation of emissions, emission standards for vehicles and intersectoral collaboration (UNEP, 2015 [6]). However, most developing countries, such as Egypt, lack the local infrastructure to access detailed information on technical factors such as energy consumption, fuel type and technology, leading to discrepancies in inventories (Xue et al., 2012 [7]). As a consequence, the monitoring of emissions, which is important to evaluate the effects of the air pollution control policies, is of limited reliability.

To overcome the uncertainties in the emission inventories, the use of independent observations systems is becoming increasingly prevalent. In this study, we investigate the use of satellite remote sensing of atmospheric concentrations to improve the quantification of NO_x emissions in Egypt. Spectrally resolved satellite measurements of solar backscattered radiation enable the quantification of NO_2 and other trace gases absorbing in the UV-Visible spectral range based on their characteristic spectral absorption patterns. Tropospheric vertical column densities, i.e. vertically integrated NO_2 concentrations in the troposphere, have been providing information on the spatial distribution of tropospheric NO_2 at global scale for nearly 30 years, allowing the identification of different sources of NO_x and the quantification of the associated emissions (Leue et al., 2001 [8]; Martin et al., 2003 [9]; Mijling and van der A, 2012 [10]; de Foy et al., 2015 [11]; Goldberg et al., 2019 [12]; Beirle et al., 2019 [13]; Lorente et al., 2019 [14]; Lange et al., 2021 [15]). In October 2017, the Sentinel-5 Precursor satellite was launched. Its main instrument is the TROPOspheric Monitoring Instrument (TROPOMI), which provides tropospheric NO_2 column densities at a high spatial resolution, with a large swath width and with a daily frequency (Veefkind et al., 2012 [16]). By applying the steady-state continuity equation (Beirle et al., 2019 [13]; Lama et al., [17], 2020), it is possible to build a top-down model that directly quantifies NO_x emissions from these NO_2 column densities, provided that some key parameters (wind, temperature, hydroxyl radical concentration and concentration ratio between NO_x and NO_2) are correctly estimated. This model is used to quantify the anthropogenic NO_x emissions in Egypt for a 2-year period, from November 2018 to November 2020.

This paper is organised as follows: Section 2 provides a description of the datasets used in this study. Section 3 explains the build-up and the limits of the top-down model used to quantify NO_x emissions in Egypt. It also presents a method for validating the parameters of the model by using NO_2 line density profiles over Riyadh, Saudi Arabia. Section 4 presents the analysis of this validation method. It presents the location of the main NO_x sources in Egypt and evaluates the vertical sensitivity of the model. It also assesses the ability of the model to show less human activity on Fridays and during the lockdown that took place during the COVID-19 pandemic. It finally confronts the inferred emissions with different inventories in terms of amplitude and seasonality. Section 5 presents our conclusion and general remarks.

2 Instrumentation and data

2.1 TROPOMI NO_2 retrievals

The TROPOspheric Atmosphere Monitoring Instrument (TROPOMI), onboard the European Space Agency's (ESA) Sentinel-5 Precursor (S-5P) satellite, provides measurements for atmospheric composition. TROPOMI is a spectrometer observing wavelengths in the infrared, visible and ultraviolet light at around 13:30 local time. The UV-Visible spectral band at 405-465 nm is used to retrieve NO_2. Other spectral bands are used to observe methane, formaldehyde, sulphur dioxide, carbon monoxide and ozone, as well as aerosols and cloud physical properties. The very high spatial resolution offered by TROPOMI (originally 3.5×7 km^2 at nadir, improved to 3.5×5.5 km^2 since 6 August 2019) provides unprecedented information on tropospheric NO_2. Its large swath width ($\sim$ 2600 km) enables to construct NO_2 images on large spatial scales. Those images greatly improve the potential for detecting highly localised pollution plumes above the ground, identifying small-scale emission sources but also estimating emissions from megacities, industrial facilities and biomass burning. We use TROPOMI NO_2 retrievals from November 2018 to November 2020 over the Middle East and Eastern Mediterranean region, and more specifically over Egypt and the city of Riyadh, Saudi Arabia. The arid climate of this region offers a large number of clear-sky days throughout the year, but also the presence of large plumes of pollutants due to a large human concentration along rivers and around megacities, which allows us to observe high NO_2 concentrations in the region with a high signal-to-noise ratio. To facilitate data

https://doi.org/10.5194/acp-2021-1051
Preprint. Discussion started: 10 January 2022

Atmospheric Chemistry and Physics Discussions

filtering, TROPOMI products provide a quality assurance value q_a. This value ranges from 0 (no data) to 1 (high-quality data). For our analysis of concentrations, we selected NO_2 retrievals with q_a values equal to or greater than 0.75, which systematically correspond to clear-sky conditions (Eskes and Eichmann, 2019 [18]). TROPOMI soundings are gridded for this study at a spatial resolution of $0.1^\circ \times 0.1^\circ$ with daily coverage.

2.2 Wind data

The horizontal wind information $\mathbf{w} = (u, v)$ is taken from the European Centre for Medium-Range Weather Forecasts (ECMWF) ERA5 data archive (fifth generation of atmospheric reanalyses) at a horizontal resolution of $0.25^\circ \times 0.25^\circ$ on 37 pressure levels (Hersbach et al., 2020 [19]). The hourly values have been linearly interpolated to the TROPOMI orbit timestamp and re-gridded with a $0.1^\circ \times 0.1^\circ$ resolution.

2.3 CAMS real-time fields

The Copernicus Atmospheric Monitoring Service (CAMS) global near-real-time service provides analyses and forecasts for reactive gases, greenhouse gases and aerosols on 25 pressure levels with a horizontal resolution of $0.4^\circ \times 0.4^\circ$ and a temporal resolution of 3 hours (Huijnen et al., 2016 [20]). For the calculation of NO_x emissions from TROPOMI observations, we use CAMS concentration fields of nitrogen oxides (NO and NO_2) and hydroxyl radical (OH). We also use CAMS temperature field T. NO and NO_2 concentrations are used to account for chemical processes that take place in polluted air. Anthropogenic activities produce mainly NO, which is transformed into NO_2 by reaction with ozone O_3. NO_2 is then photolyzed during the day, reforming NO and producing an oxygen atom O (Seinfeld, 1989 [21]). This photochemical equilibrium between NO and NO_2 can be highlighted with the NO_x:NO_2 concentration ratio, whose value depends on local conditions, allowing to perform a conversion from NO_2 production to NO_x emissions. The reason for the use of OH is different. OH is the main oxidant that controls the ability of the atmosphere to remove pollutants such as NO_2 (Logan et al., 1981 [22]). It is mainly produced during daylight hours by interaction between water and atomic oxygen produced by ozone dissociation (Levy, 1971 [23]). In air that is directly influenced by pollution, the second source of OH is due to a reaction between NO and HO_2. This reaction, referred to as the NO_x recycling mechanism, illustrate the nonlinear dependence of the OH concentration on NO_2 (Valin et al., 2011 [24]; Lelieveld et al., 2016 [25]). Since the OH lifetime is typically of less than a second, its concentration in the troposphere is very low and difficult to measure. As a consequence, global analyses, which estimate OH concentrations from other variable species (Li et al., 2018 [26]; Wolfe et al., 2019 [27]), provide a natural representation for OH concentrations, but with high associated uncertainties. Therefore, the CAMS OH concentrations are used here to account for the NO_2 oxidation to form nitric acid (HNO_3), whose representation is explained in Section 3.1. Finally, the temperature field is used to control variations in the kinetic parameters (Burkholder et al., 2020 [28]). The hourly values are also linearly interpolated to the TROPOMI orbit timestamp and re-gridded with a $0.1^\circ \times 0.1^\circ$ resolution.

2.4 Calculation of urban enhancements

Detecting traces of anthropogenic emissions in TROPOMI NO_2 images is not a straightforward process. The NO_2 signal from a sparsely populated area or a small industrial plant may be covered by numerical noise or by the signal generated by natural sources such as lightning (Boersma et al., 2005 [29]) and soil emissions (Yienger et al., 1995 [30]). It is therefore necessary to remove the natural part of the atmospheric signal from the detected NO_2 enhancement. With an atmospheric lifetime of about a few hours, the presence of NO_2 is relatively short. Consequently, the majority of NO_2 is not transported far downwind from its sources. Thus, near-surface NO_2 concentrations are generally high over industrial facilities and densely populated areas that need to be identified. Because Egypt's population is almost entirely located along the Nile River and its delta, the study of NO_x emissions in this country cannot therefore be reduced to the study of a small number of point sources, as it would be the case for several other parts of the region, and must be carried out in the form of a mapping of the country. Further explanation is provided in Section 3.3. To identify urban or industrial areas in Egypt, we use the Socioeconomic Data and Applications Center (SEDAC) GRUMP (Global Rural-Urban Mapping Project) data archive, which comprises eight global datasets, including a population density grid provided at a resolution of 30 arc seconds, with population estimates normalised for the year 2000 (CIESIN, 2019 [31]). We combine this database with field data giving the location of industrial facilities from energy-intensive industries in the region (data have been retrieved from Global Energy Observatory for oil and gas-fired power plants, from IndustryAbout for aluminium, steel and iron plants, from the work of Elvidge et al., 2016 [32] for flaring sites, and from the work of Steven J. Davis and Dan Tong for cement plants, links are given at the end of this article).

https://doi.org/10.5194/acp-2021-1051
Preprint. Discussion started: 10 January 2022

Atmospheric Chemistry and Physics Discussions

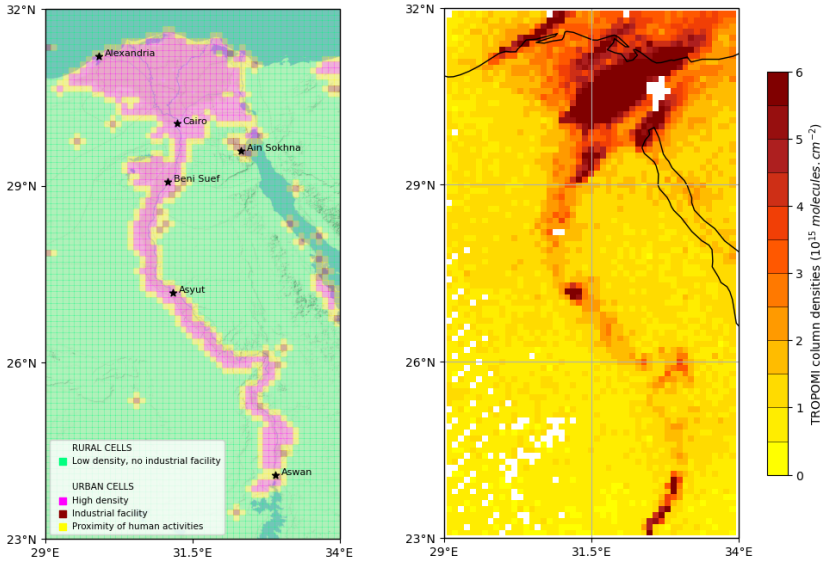

Figure 1: (left) Part of Egypt centered on Nile river. Pink cells represent locations with an average human density above 100 hab.km^{-2}, brown cells represent locations with industrial facilities outside cities, and yellow cells represent locations in the vicinity of pink and brown cells. Green cells represent areas which do not correspond to any of the three criteria, considered to be void of human activity. Five larges cities in the country and the industrial area of Ain Sokhna are denoted with stars. (right) TROPOMI observation of NO_2 column densities above Nile valley on 3 January 2019. White pixels correspond to areas with low quality data ($q_a < 0.75$) or no data.

These datasets are used to remove the non-anthropogenic part of the NO_x emissions signal. We conduct this removal by subtracting the mean emissions over desert and rural areas from the mean emissions over urban and industrial areas. In order to perform this distinction between two types of areas, our study is carried out using a grid with a resolution of $0.1° \times 0.1°$ characterised by two types of cells. A cell is considered "urban" if it has a population density higher than a threshold of 100 hab.km^{-2}, or if its centre is close to an industrial facility. Otherwise, the cell is considered "rural". In order to avoid any smearing that would correspond to abnormally high emissions outside urban areas (which can happen if the wind is poorly estimated), transition cells (in the immediate vicinity of the mentioned urban cells) are also considered to be urban. Figure 1 shows the distinction between urban and rural cells on our domain in Egypt that lies between parallels 23°N and 32°N and meridians 29°E and 34°E. Most urban cells are located in the Nile area. Some urban cells are also found on the coast or in isolated parts in the desert. They correspond to remote industrial facilities, including major flaring sites, or sparsely populated industrial centres such as Ain Sokhna's industrial area. The domain comprises $n_{rur} = 3692$ rural cells and $n_{urb} = 949$ urban cells. The resulting grid is conveniently used as a mask for the urban enhancement, whose calculation is explained in Section 3.4.

2.5 Emission inventories

We compare TROPOMI-derived NO_x emissions to the Emissions Database for Global Atmospheric Research (EDGARv5.0) for 2020 and the CAMS global anthropogenic emissions (CAMS-GLOB-ANT_v4.2) inventory released in 2020. Both datasets provide $0.1° \times 0.1°$ gridded emissions for different sectors on a monthly basis. EDGARv5.0 (Crippa et al., 2019 [33]) is based on activity data (population, energy production, fossil fuel extraction, industrial processes, agricultural statistics, etc.) derived from the International Energy Agency (IEA) and the Food and Agriculture Organization (FAO), corresponding emission factors, national and regional information on technology mix data and end-of-pipe measurements. The inventory covers the years 1970-2015. CAMS-GLOB-ANT_v4.2 (Granier et al., 2019 [34]) is developed within the framework of the Copernicus Atmospheric Monitoring Service. Its NO_x emissions are based on various existing sectors in the EDGARv4.3.2 emissions from 2000-2012 and are extrapolated to the current year using 2011-2014 sector-based trends from the Community Emissions Data System (CEDS) inventory (Hoesly et al., 2018 [35]). From one inventory to another, the names of the sectors may vary. In EDGARv5.0 and CAMS-GLOB-ANT_v4.2, the emissions for a given country are derived from the type of technologies used, the dependence of emission factors on fuel type, combustion conditions, as well as activity data and low resolution emission factors (Janssens-Maenhout et al., 2019 [36]).

https://doi.org/10.5194/acp-2021-1051
Preprint. Discussion started: 10 January 2022

Atmospheric Chemistry and Physics Discussions

3 Method

3.1 Calculation of NO_2 production from TROPOMI observations

As a first step, we use TROPOMI's tropospheric NO_2 columns Ω_{NO_2} to derive top-down NO_2 production maps. Using the horizontal wind $\mathbf{w}$, the NO_2 flux is given as $\Omega_{NO_2}\mathbf{w}$. The divergence of this flux is added to the local time derivative $\frac{\partial \Omega_{NO_2}}{\partial t}$ to balance NO_2 sources e_{NO_2} and sinks s_{NO_2} according to the continuity equation:

$$\frac{\partial \Omega_{NO_2}}{\partial t} + \mathrm{div}(\Omega_{NO_2}\mathbf{w}) = e_{NO_2} - s_{NO_2} \quad (1)$$

In steady state, the time derivative disappears and the mass balance is reduced to three terms. The sources of NO_2 can be estimated by taking the combined effect of atmospheric transport losses and the different sinks. For the transport term, we calculate numerical derivatives with a fourth-order central-finite difference formula at each point of the domain. For the sink term, since the local overpass time of TROPOMI occurs is in the middle of the day, NO_2 losses are largely dominated by the three-body reaction involving NO_2 and OH (Seinfeld, 1989 [21]). Two channels have been identified for this reaction (Burkholder et al., 2020 [28]), leading to the production of nitric acid HNO_3 and pernitrous acid HOONO:

$NO_2 + OH + M \rightarrow HNO_3 + M$

$NO_2 + OH + M \rightarrow HOONO + M$

No corrections are made to the TROPOMI observations. Slant column densities are used as vertical densities. This use amounts to neglect the air mass factor, which is a source of structural uncertainty in NO_2 retrievals (Boersma et al., 2004 [37]; Lorente et al., 2017 [38]). In polluted environments, this source of uncertainty becomes non-negligible. Rather than calculating the air mass factor, we take this factor into account in the final uncertainty estimates. The corresponding uncertainty level is given in Section 4.7. For the OH concentrations that are considered in this region (1-30 $\times 10^6$ molecules.cm^{-3}), the reactions above follow first order kinetics. The total sink term can therefore be calculated as $s_{NO_2} = \Omega_{NO_2}/\tau$ with:

$$\tau = \frac{1}{k_{mean}(T, [\mathrm{M}]) \cdot [\mathrm{OH}]} \quad (2)$$

τ appears here as the characteristic mixed lifetime of NO_2 in the atmosphere. The value of the reaction rate k_{mean} characterises the reactions between NO_2 and OH and depends on atmospheric conditions (temperature T and total air concentration [M]). We calculate the value of k_{mean} using a temperature-dependent analytical formula for different pressure ranges (Burkholder et al., 2020 [28]). Note that although this reaction rate accounts for both reactions with OH, the second channel is minor and cannot be considered as a true NO_x sink, HOONO being rapidly decomposed back to NO_2 and OH in the lower troposphere (Sander et al., 2011 [39]). The value of k_{mean} therefore represents the total loss of NO_2 due to OH and cannot be used to infer HNO_3 and HOONO production. Thus, the NO_2 production can be calculated as the sum of a transport term and a sink term:

$$e_{NO_2} = \mathrm{div}(\Omega_{NO_2}\mathbf{w}) + \Omega_{NO_2}/\tau \quad (3)$$

The treatment for NO_x removal is simplified here. In reality, NO_x concentrations are influenced by other sinks. At the global scale, the other important sinks are:

- NO_2 deposition through the leaf stomata of vegetation (Delaria et al., 2020 [40]);
- NO_x oxidation by organic radicals to produce of alkyl and multifunctional nitrates (Sobanski et al., 2017 [41]; Romer Present et al., 2020 [42]);
- NO reaction with HO_2 to produce nitric acid (Butkovskaya et al., 2005 [43]), whose yield is strongly enhanced in presence of water vapour (Butkovskaya et al., 2009 [44]);
- NO conversion to NO_3, the latter being in thermal equilibrium with NO_2 and N_2O_5;
- NO_2 reversible reaction with peroxyacetyl radical to produce peroxyacetylnitrate (Moxim et al., 1996 [45]);
- NO_2 uptake onto black carbon particles (Longfellow et al., 1999 [46]).

Stavrakou et al., 2013 [47] has shown that the reaction between NO_2 and OH forming HNO_3 accounted for 26 to 64% of total NO_x emissions at the global scale. However, the features of the climate in Egypt during daytime hinder many other sinks to significantly take place. Losses due to deposition and the formation of alkyl and multi-functional nitrates are thus considered insignificant in Egypt where the forest cover is totally negligible. We also neglect the reaction between NO and HO_2 as the corresponding reaction rate is weakened by a factor 3 to 8 in dry conditions (Butkovskaya et al., 2005 [43]). The formation of NO_3 and N_2O_5 via heterogeneous processes, which has a significant contribution during nighttime in the Mediterranean region (Friedrich et al., 2021 [48]), is neglected at 13:30 when OH

https://doi.org/10.5194/acp-2021-1051
Preprint. Discussion started: 10 January 2022

Atmospheric Chemistry and Physics Discussions

is almost at its daily maximum. Similarly, the production of PAN, which peaks in late afternoon and early evening (Seinfeld, 1989), is neglected at 13:30. Finally, the uptake of NO_2 onto black carbon is of limited amount in the Mediterranean region (Friedrich et al., 2021 [48]). All these processes being neglected, the reaction between NO_2 and OH is the only sink that is considered in our calculations to provide a reliable indication of NO_x emissions.

3.2 Interpolation to daily average emissions

All parameters are evaluated at 13:30 local time, which means NO_2 production is calculated for the same moment. In Egypt, the maximum and minimum electricity consumption are reached around 20:00 and 6:00 local time respectively, and inter-daily consumption differences have been weakened by the increasing sales of air conditioning and ventilation systems in the past decades (Attia et al., 2012 [49]). The national average daily load profiles provided by the National Egyptian Electricity Holding Company show that the mean daily electricity consumption corresponds approximately to the consumption at 13:30 in the country (EEHC, 2021 [50]). The difference between the two quantities being very small both in summer (about +2 to -3%) and winter (about -2 to -6%), we neglect this difference and consider our inferred emissions as representative of the average activity in Egypt at any time of the year.

3.3 Validation of CAMS OH concentration using line density calculations for Riyadh

When the transport term is integrated over large spatial scales, it cancels out due to the mass balance in the continuity equation between NO_2 sources and NO_2 sinks. At first order, the integration of the inferred emissions over the whole domain (of about 450,000 km^2) thus reflects chemical losses of the sink term. In this term, the NO_2 lifetime calculation involves the reaction rate k_{mean}, whose annual variability is low due to small changes in Egyptian midday temperatures throughout the year, and OH concentration, whose annual variability is highly marked. In Egypt, tropospheric OH concentrations, which are strongly correlated with solar ultraviolet radiation (Rohrer and Berresheim, 2006 [51]) and NO_x emissions, are higher in summer than in winter. To ensure an adequate representation of the OH field by CAMS data, we select a large number of TROPOMI images characterised by a homogeneous wind field, in which we calculate the NO_2 lifetime according to Equation (2), where [OH] corresponds to the near-real-time CAMS data and k_{mean} is calculated with the formula from Burkholer et al., 2020 [28]. We compare this value with the lifetime determined by a method initially developed by Beirle et al., 2011 [52], and expanded by Valin et al., 2013 [53] by introducing a rotation of the image to refine the chemical lifetime. This method consists in fitting an exponentially modified Gaussian function (EMG) to NO_2 line density profiles. These profiles correspond to the NO_2 mean value along the mean wind direction in the pollution pattern and centered around the source. They are obtained by rotating TROPOMI images in the mean wind direction and averaging the values of the nearest columns in a 100 km^2 area. Line density profiles are generated on a distance of 300 km. An example is given in Figure 3. Within the average profile, the NO_2 burden and lifetime can be derived from the parameters that describe the best statistical fit. The EMG model is expressed as follows (Lange et al., 2021 [15]):

$$\langle \Omega_{NO_2} \rangle (x|B, A, x_0, \mu, \sigma) = B + \frac{A}{2x_0} \exp\left(\frac{\mu - x}{x_0} + \frac{\sigma^2}{2x_0^2}\right) \mathrm{erfc}\left(-\frac{1}{\sqrt{2}}\left(\frac{x-\mu}{\sigma} - \frac{\sigma}{x_0}\right)\right) \quad (4)$$

Here, x is the distance in the downwind-upwind direction, B is the NO_2 background, A is the total number of NO_2 molecules observed in the vicinity of the point source, x_0 is the e-folding distance downwind, representing the exponential length scale of NO_2 decay, μ is the location of the apparent source relative to the centre of the point source, and σ is the standard deviation of the Gaussian function, representing the length scale of Gaussian smoothing. Using a non-linear least squares fit, we estimate the five unknown parameters: A, B, x_0, μ and σ. Using the mean zonal wind module $\sqrt{\mathbf{w}^2}$ of the NO_2 line density domain, the mean effective NO_2 lifetime τ_{fit} can be estimated from the fitted parameters:

$$\tau_{\mathrm{fit}} = \frac{x_0}{\langle \sqrt{\mathbf{w}^2} \rangle} \quad (5)$$

The geography of Egypt does not suit the method described here. The Egyptian population is contiguously concentrated along the Nile, which makes it difficult to define point sources isolated from human activity. Furthermore, large isolated cities such as Alexandria or Suez are too close to the coast for the wind to be considered homogeneous. We therefore use the nearby city of Riyadh, Saudi Arabia (24.684°N, 46.720°E) to perform the comparison between the CAMS-induced lifetime and the fit-induced lifetime. Riyadh is particularly suitable for several reasons. Firstly, Riyadh is a city within the latitudinal extend of Egypt (1600 km from Cairo), has a climate which is similar to the typical Egyptian climate. Second, NO_2 tropospheric columns over Riyadh are high ($\sim 9 \times 10^{15}$ molecules.cm^{-2}),

https://doi.org/10.5194/acp-2021-1051
Preprint. Discussion started: 10 January 2022

Atmospheric Chemistry and Physics Discussions

leading to retrievals with a high signal-to-noise ratio. Third, Riyadh is far from the coast, and its flat terrain makes the surrounding wind fields rather homogeneous during most of the year.

As the fitting algorithm is very sensitive to any disturbance that might be induced by NO_2 production from other point sources, it is necessary to identify heavy industrial facilities in the area. As Riyadh is also an industrial area, many power plants are located close to the city centre. Figure 2 shows the location of the most important emitters in the region, which include five gas-fired power plants (PP7, PP8, PP9, PP10 and PP14), one oil-fired power plant (PP4) and one cement plant (CP). The five gas power plants, with a total capacity of more than 10 GWe, are located in the periphery of the city. These power plants are sufficiently far away from the city centre for TROPOMI to distinguish their own emissions from those of Riyadh's centre itself with a resolution of $0.1° \times 0.1°$, which is not the case for CP and PP4 which are located in the city centre. It is therefore appropriate to restrict the study of NO_2 patterns over Riyadh to days for which the emissions from the city centre and those from the gas power plants do not mix. This is the case when the wind blows steadily and homogeneously in a north-south direction. Within about 150 km around the city centre, we thus calculate the average zonal wind given by ERA5 and consider the observation as reliable if the mean angle $\langle\theta\rangle$ of the observations deviates by less than 40° from the north or the south, with a standard deviation σ_θ of less than 36°. This condition generally leads to a selection of observations with large wind speeds, low winds speeds being often associated with more variable directions. This ensures the NO_2 decay to be dominated by chemical removal and not by the variability of the wind (Valin et al., 2013 [53]). Finally, we select observations with clear-sky conditions downstream of the flow (with at least 80% downstream cells with $q_a > 0.75$).

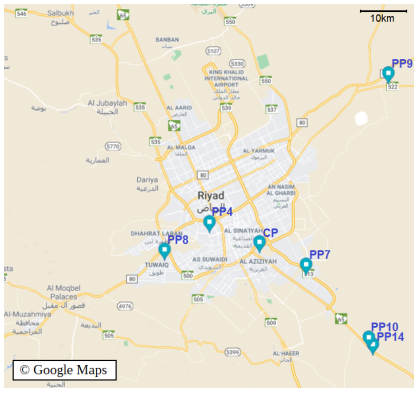

Figure 2: Map of Riyadh's city centre with its surrounding power plants (PP4, 7, 8, 9, 10 and 14) and cement plant (CP). The map has been extracted from © Google Maps.

Our $0.1° \times 0.1°$ gridding ensures that retrieved lifetimes are governed by physical decay of NO_2 and not an artifact of the spatial resolution (Valin et al., 2011 [24]). The fitting procedure is very sensitive to the wind direction. Instead of manually correcting the ERA5 wind field for individual NO_2 patterns, we use another procedure: the curve fitting is performed for every sample with three different rotation angles, corresponding to the wind direction with a correction of -10, 0 or 10 degrees. A record is kept if one of these three fits leads to a determination correlation with the corresponding NO_2 line density whose coefficient is greater than 0.97. Among the remaining samples, we keep those with a value of τ_{fit} greater than 1.0 hr (considered sufficiently high to be relevant). An example of curve fitting is given in Figure 3.

The phenomena under study take place in the planetary boundary layer (PBL), which in this region has a midday height of about 2 km (Filioglou et al., 2020 [54]). TROPOMI observations only provide information on the total NO_2 content of the tropospheric column, without providing information on the vertical distribution of concentrations. Extracting emissions from concentrations therefore requires a choice on the height at which wind, temperature and OH data are taken. Lama et al., 2020 [17] and Lorente et al., 2019 [14] conducted similar studies using the boundary layer average wind, while Beirle et al., 2019 [13] chose a vertical level of about 450 m above ground. Because vertical transport of NO_x, which is emitted mainly from combustion engines and industrial stacks, is generally minor compared to horizontal transport, NO_x is confined to the first few hundred metres above ground level. Using PBL-averaged data poses a problem of consistency as wind, temperature and OH concentration values vary significantly within the PBL. As a consequence, we compare the CAMS-induced lifetime τ and the fit-induced lifetime τ_{fit} using the parameters ($\mathbf{w}$, [OH] and T) at two different vertical levels: a medium level $\mathcal{A}$ at 925 hPa (about 770 m above ground level), and

https://doi.org/10.5194/acp-2021-1051
Preprint. Discussion started: 10 January 2022

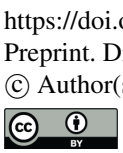

Atmospheric Chemistry and Physics Discussions

a bottom level $\mathcal{B}$ at 987.5 hPa (about 210 m). These levels are interpolated from four and two ECMWF or CAMS consecutive pressure levels respectively (1000-850 hPa for level $\mathcal{A}$ and 1000-975 hPa for level level $\mathcal{B}$). Most urban cells having an altitude between 0 and 150 m, the corresponding pressure variations are small (up to $\sim$ 16 hPa), which allows us to neglect the effects of topography on the position of pressure levels. Figure 4 sums up the selection method for the comparison of methods.

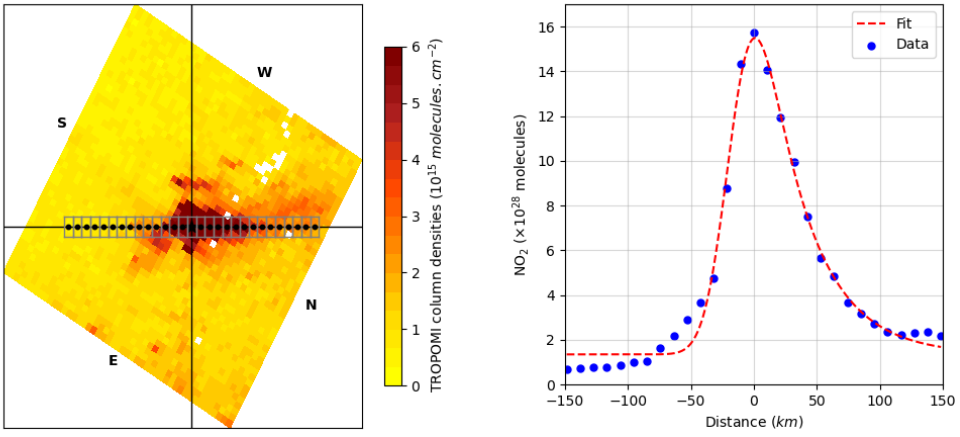

Figure 3: Estimation of the NO_2 lifetime from a pattern above Riyadh on 03/08/2020: (left) NO_2 plume rotated with its wind direction around the source (cross) to an upwind-downwind pattern. Grey boxes centered around black points indicate the spatial extent in the spatial integration of NO_2 columns to obtain the NO_2 line density. Values of cardinal points are noted in black. (right) Line densities (points) representing the downwind evolution of NO_2 as function of the distance to Riyadh city centre, and the corresponding fit according to the exponentially modified Gaussian function (dashed line).

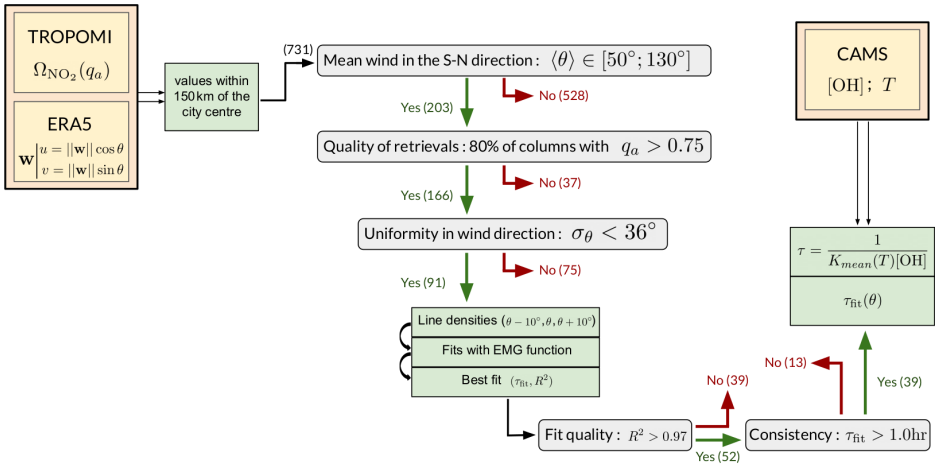

Figure 4: Selection method for NO_2 patterns over Riyadh. Datasets (yellow-orange) are used to calculate the quantities (light green) that are submitted to different tests (grey). 731 patterns are progressively conserved (green arrows) or rejected (red arrows). At each stage, the number of conserved or rejected patterns are noted within brackets (the value is only given for calculations performed at level $\mathcal{B}$). This selection process compares the lifetimes estimated by the EMG function fitting with TROPOMI line density profiles to the lifetimes calculated according to Equation (2) with CAMS data.

3.4 Calculation of anthropogenic NO_x emissions and comparison with inventories

We calculate NO_x emissions on the entire domain from NO_2 production by using CAMS NO and NO_2 concentrations. These quantities are not intended to replace TROPOMI observations; they are used to apply the concentration ratio

https://doi.org/10.5194/acp-2021-1051
Preprint. Discussion started: 10 January 2022

Atmospheric Chemistry and Physics Discussions

$[NO_x]/[NO_2] = ([NO]+[NO_2])/[NO_2]$ to account for the conversion of NO_2 to NO and vice versa. As NO concentrations in urban areas generally range from 2 to 10 ppb, the characteristic stabilization time of this ratio ranges from 4 to 20 minutes (Graedel et al., 1976 [55]; Seinfeld and Pandis, 2006 [56]). This time being lower than the order of magnitude of the inter-mesh transport time (about 30 min considering the resolution used and the mean wind module in the region), we can reasonably neglect the effect of the stabilization time of the conversion factor on the total composition of the emissions and treat each cell of the grid independently from its neighbours. Beirle et al., 2019 [13] found an annual average of 1.32 for this conversion factor, but CAMS data shows small deviations from this value over Egyptian urban areas, as urban concentrations depend on local conditions. We therefore calculate for each cell of the domain the following equation:

$$e_{NO_x} = \frac{[NO_x]}{[NO_2]} e_{NO_2} \tag{6}$$

For convenience, quantities $\frac{[NO_x]}{[NO_2]}\mathrm{div}(\Omega_{NO_2}\mathbf{w})$ and $\frac{[NO_x]}{[NO_2]}\Omega_{NO_2}/\tau$ represent the respective contributions of the transport and the sink terms to total NO_x emissions. We obtain the emissions related to human activity at the scale of the country by removing the influence of the NO_2 background detected by TROPOMI and the possible non-anthropogenic sources of NO_x. Neglecting the part of the country that lies outside the domain, the average surface emissions from Egypt's anthropogenic activity E_{NO_x} can be calculated as being the difference between NO_x emissions over all urban cells and NO_x emissions over all rural cells:

$$E_{NO_x} = \frac{1}{n_{urb}} \sum_{i=1}^{n_{urb}} e_{NO_x,i} - \frac{1}{n_{rur}} \sum_{j=1}^{n_{rur}} e_{NO_x,j} \tag{7}$$

For robust statistics, these derived emissions can be averaged monthly, enabling a month-by-month comparison with bottom-up inventories. The linearity of the averaging processes ensures the interchangeability of temporal and spatial averages. A monthly average is relevant because it aggregates enough data to limit the high inter-day variability due to changing wind patterns or differences between week days and week-ends. In addition, it enables the study of monthly NO_x emission profiles which reflect changes in human activities throughout the year due to temperature changes, economic constraints and cultural norms. The use of the average value for rural cells as a "background" that is subtracted from the emission estimates for urban cells assumes that all natural processes in NO_x emissions lead to similar amounts for both types of cells, which is not trivial, as the vast majority of rural cells are located in desert, mountainous or oceanic areas while the vast majority of urban cells are located near the Nile valley or the Mediterranean coast. However, as the processes involved in natural NO_x sources lead to emissions smaller than anthropogenic emissions in polluted areas (e.g. Lin, 2012 [57] for China), we neglect this difference in the following calculations. Finally, the total anthropogenic NO_x emissions of the domain can be obtained by multiplying E_{NO_x} by the cumulative area covered by the urban cells (approximately 95,000 km^2).

4 Results and discussion

4.1 Line densities and NO_2 lifetime

Here we compare the results of the TROPOMI line densities fits for Riyadh to the lifetime calculated by Equation (2) using CAMS data. The two years of TROPOMI observations (from November 2018 to November 2020) provide a wide variety of profiles. For level $\mathcal{B}$, Figure 4 also provides the number of samples that are being kept at each stage of the process. Of the 731 observations available, 203 have a wind direction in the cone with a north-south orientation with an aperture of 40° (i.e. between 340° and 20° or between 160° and 200°). Of the remaining observations, 166 have a sufficiently clear sky to be retained. The criterion of weak variability for the wind direction brings to 91 the number of observations that are kept by the method. On these 91 observations, the line density profiles are calculated and the fits applied. According to Equation (5), the lifetime is calculated using the mean wind module around the point source. The two lifetimes are calculated with the parameters taken at the medium level $\mathcal{A}$ or at the top level $\mathcal{B}$. Of the 91 fits obtained, 52 are of high quality (correlation coefficient between fit function and line density profile greater than 0.97) for level $\mathcal{A}$ and 51 for level $\mathcal{B}$. 39 of these fits lead to a lifetime τ_{fit} greater than 1.0 h for both levels (they do not necessarily correspond to the same days). All remaining samples correspond to atmospheric conditions with moderate to fast winds, with a module ranging between 2 and 11 m/s (with an average of 5.9 m/s) for level $\mathcal{A}$ and between 3 and 8 m/s (with an average of 5.4 m/s) for level $\mathcal{B}$.

https://doi.org/10.5194/acp-2021-1051
Preprint. Discussion started: 10 January 2022

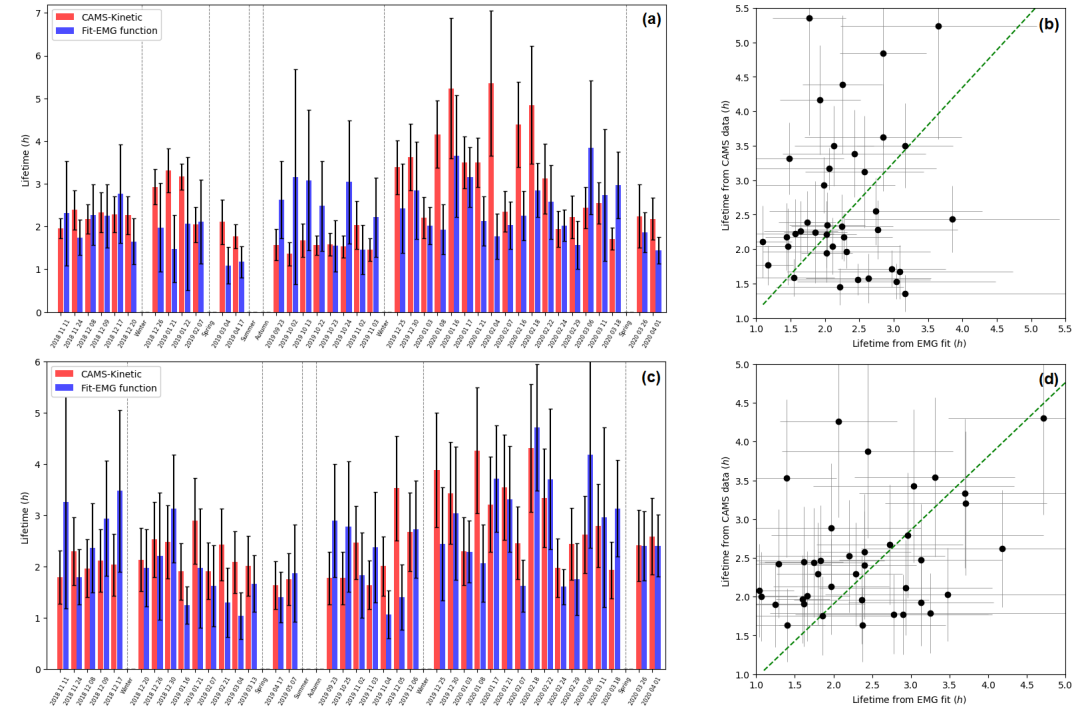

Figure 5: (left) Comparison between CAMS-induced NO_2 lifetimes and lifetimes from NO_2 line density fittings with EMG function above Riyadh city centre, for level $\mathcal{A}$ (a) and $\mathcal{B}$ (c). The samples presented correspond to patterns in clear-sky conditions for which the mean wind is in the north-south direction with a low variance, and for which the correlation between line density profile and fit gives a correlation coefficient of more than 0.97 and a lifetime of more than 1.0 h. No NO_2 patterns during the summers of 2019 and 2020 meet these conditions. Dashed lines separate the groups of observations by season. (right) Comparison between the two calculated lifetimes for level $\mathcal{A}$ (b) and $\mathcal{B}$ (d). A linear regression with an intercept forced to be zero is displayed with a green dashed line.

These lifetimes are compared to the corresponding lifetimes obtained from CAMS data in Figure 5 for each sample, which is divided into seasons for a more convenient comparison. The use of level $\mathcal{A}$ leads to a notable underestimation of the NO_2 lifetime in autumn compared to the lifetime calculated with the fitting method. This same level leads to an overestimation of the lifetime in winter. This trend is not found with the use of level $\mathcal{B}$, which leads to a better reproduction of the lifetimes calculated with the fitting method for the available seasons. Figure 5 shows a linear regression between the two calculated lifetimes. The results are scattered, with a correlation coefficient higher for level $\mathcal{B}$ (0.376) than for level $\mathcal{A}$ (0.139). When the intercept of the regression line is forced to zero, the resulting slope is closer to 1 for level $\mathcal{B}$ (0.953) than for level $\mathcal{A}$ (1.086). Level $\mathcal{B}$ is therefore the one that leads to the best match between the lifetime calculated with Equation (2) and the lifetime calculated from line densities. The results that are presented in the following sections (except for Section 4.3) are therefore results of calculations performed with parameters ($\mathbf{w}$, [OH], T and $[NO_x]/[NO_2]$) estimated at level $\mathcal{B}$. Nevertheless, it should be noted that no summer observations were included in the comparison. The main reason for this is the wind direction: of the 188 summer days observed, 178 of them have a mean wind direction outside the north-south cone over central Riyadh. On the remaining ten days (one for summer 2019 and nine for summer 2020), the ERA5 wind direction is too variable for the fit to be considered relevant, or the fit results in a correlation coefficient below 0.97. Thus it is not clear how correctly the NO_2 lifetime would be calculated during both summer periods by Equation (2). OH concentrations being the main driver of this lifetime, we cannot assess the relevance of the representation of OH concentrations by CAMS data during summer days in the study.

4.2 Mapping of Egypt's NO_x emissions

The top-down emission model is then applied to the Egyptian domain with CAMS OH concentration and temperature fields for lifetime calculations. For each cell, NO_x emissions are calculated according to Equation (6), resulting in a mapping of Egypt's emissions. The obtained values are averaged monthly from November 2018 to November 2020.

https://doi.org/10.5194/acp-2021-1051
Preprint. Discussion started: 10 January 2022

Atmospheric Chemistry and Physics Discussions

Figure 6 shows a composition of the emissions map with the transport term and the sink term for the months of January and July 2019. The Nile appears on transport term maps: the divergence calculation complies with what is expected from a line density of emitters, i.e. a clear separation of zones of positive divergence from zones of negative divergence with a separation line corresponding to the course of the river. The fact that the negative divergence zones are located to the east of the river and the positive divergence zones to the west is the result of the wind being predominantly towards in the northeast and southeast quadrants during the overflight of the region. Some point sources like Cairo, Alexandria, Asyut or Aswan are easily identifiable. The sink term, directly proportional to the TROPOMI slant column densities, also highlights these cities. However, unlike the transport term, which has a similar spatial pattern from month to month, the sink term is clearly stronger in summer than in winter. This is mainly due to a higher lifetime in winter than in summer (4.00 h on average in January 2019 and 2.15 h in July 2019) while the average TROPOMI NO_2 concentrations are slightly higher during winter (1.687×10^{15} molecules.cm^{-2} for January 2019 and 1.440×10^{15} molecules.cm^{-2} for July 2019). Over the whole domain, the mean transport term varies throughout the studied period between -0.035×10^{15} molecules.cm^{-2}.h^{-1} (January 2019) and 0.026×10^{15} molecules.cm^{-2}.h^{-1} (May 2020). Thus, it hardly contributes to the NO_x emission budget, the mean chemical sink term alone varying between 0.451×10^{15} molecules.cm^{-2}.h^{-1} (January 2020) and 1.121×10^{15} molecules.cm^{-2}.h^{-1} (September 2020).

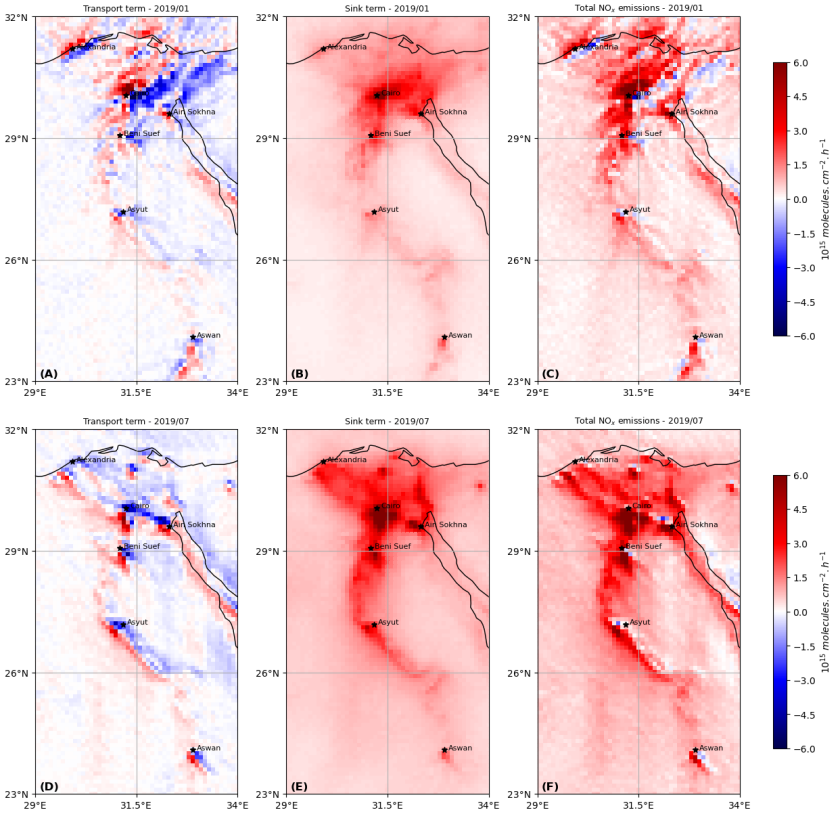

Figure 6: Construction of NO_x emissions above most of Egypt's territory: (top) transport term (A), sink term (B) and the resulting surface emissions, being counted as total emissions (C) for January 2019. (bottom) transport term (D), sink term (E) and the resulting surface emissions (F) for July 2019.

Several cities in the country are thus highlighted as the main emitters of the country, such as Cairo, Alexandria, Beni Suef, Asyut or Aswan. The industrial area of Ain-Sokhna, located southwest of Suez, also appears as a main emitter. Table 1 compares the monthly values for the sink term and the absolute value of the transport term above five major cities of the country, with populations ranging from 193,000 to 19 million inhabitants, as well as Ain-Sokhna's area. The mean values for TROPOMI column densities are also provided. According to the results, the capital city of Cairo

https://doi.org/10.5194/acp-2021-1051
Preprint. Discussion started: 10 January 2022

Atmospheric Chemistry and Physics Discussions

is by far the largest emitter in the country, largely due to its large population, resulting in high traffic emissions, but also to its intensive industrial activity. Alexandria, the country's second largest city, is not necessarily the second largest emitter, as its emissions are comparable to those of smaller cities such as Beni Suef or Asyut. However, the three cities concentrate a large amount of industrial activity: Alexandria hosts several oil and gas power plants and a small number of cement factories, while Beni Suef is close to several oil and gas power plants and hosts several flaring sites. Similarly, the city centre of Asyut is close to two oil and gas-fired power plants and a cement factory. This seems to indicate that industrial activity might be the main factor of NO_x emissions differences between these cities, before population size. This explains why NO_x emissions from these three cities are comparable to those of the industrial area of Ain Sokhna, which includes several cement plants, iron smelters and oil and gas plants. It might also explain why Aswan, which has a population that is comparable to Beni Suef or Asyut, but which does not have any major industrial site, has slightly lower emissions than the two other cities. Finally, the Gulf of Suez displays relatively large emissions, which might be attributed to the shipping sector, the region being a major gateway for international trade. Because it also hosts several flaring sites, these emissions might also be due to the oil and gas extraction activity.

City	Population density	Jan. 2019			Jul. 2019		
		Ω_{NO_2}	Transport	Sink	Ω_{NO_2}	Transport	Sink
	(khab/km^2)	($\mathcal{M}_{NO_2}$.cm^{-2})	($\mathcal{M}_{NO_x}$.cm^{-2}.h^{-1})		($\mathcal{M}_{NO_2}$.cm^{-2})	($\mathcal{M}_{NO_x}$.cm^{-2}.h^{-1})	
Cairo	52.2	18.016	5.615	5.520	8.331	2.901	5.883
Alexandria	3.2	5.569	2.047	1.188	2.518	0.694	2.402
Asyut	3.0	4.134	1.230	1.298	4.358	2.041	3.110
Aswan	1.6	2.615	0.431	1.521	2.175	0.555	1.532
Beni Suef	2.5	7.472	0.974	2.513	4.683	1.571	4.238
Ain Sokhna	- (industrial area)	8.159	1.585	2.548	5.216	2.012	4.737

Table 1: Comparison between the transport term and the sink term above different cities among the 20 most populous cities in Egypt, as well as the industrial region of Ain Sokhna located 45 km southwest of Suez for January and July 2019. Numbers correspond to average values within 18 km from the city centre. The value for the mean TROPOMI NO_2 column density is also given. The population density of the corresponding governorate (2020 value) is noted as a comparison. Unit $\mathcal{M}$ stands for a quantity of 10^{15} molecules (NO_2 or NO_x).

Although these cities and areas can be described as high-emission sites, the term responsible for these emissions differ from one site to the other. Figure 7 shows the contribution of the transport term (taken in absolute value) to total emissions for January and July 2019. Because wind fields are relatively homogeneous along the Nile on spatial scales of less than 100 km, NO_2 concentration gradients perceived by TROPOMI in the region mainly contribute to the increase of the transport term which can reach similar values as the sink term. Conversely, desert areas such as the Libyan Desert, the Eastern Desert and the Sinai region, (located respectively to the west, east and northeast of the Nile) show a very low value for the transport term compared to the sink term, due to the homogeneity of both the wind field and the detected NO_2 concentrations in these areas. Finally, a strong predominance of the transport term can be observed near coastal regions even without the presence of emitters nearby due to changing winds.

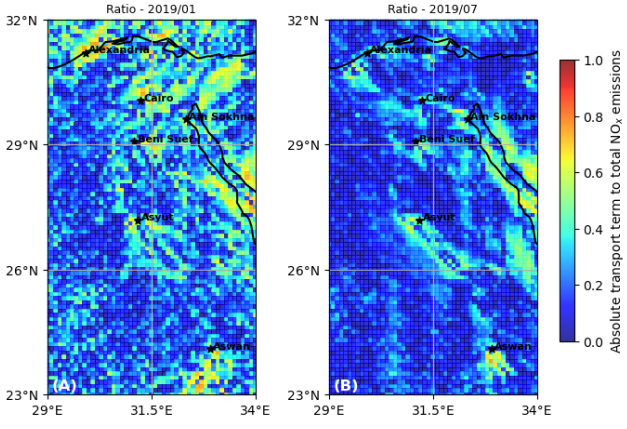

Figure 7: Share of the absolute value of the transport term in the sum of the sink term and the absolute value of the transport term above most of Egypt's territory, indicating the local importance of the transport term in NO_x emissions above urban areas. The average of this ratio is shown for January 2019 (A) and July 2019 (B).

https://doi.org/10.5194/acp-2021-1051
Preprint. Discussion started: 10 January 2022

Atmospheric Chemistry and Physics Discussions

As a consequence, most cities in the country are characterised by a transport term which can locally be of the same order of magnitude as the sink term, especially during the winter season. In the case of the Gulf of Suez, the transport term can be 1 to 2 times higher than the sink term, which varies between 0.5 and 1.0 $\times 10^{15}$ molecules.cm^{-2}.h^{-1}. Those values are slightly higher than the average emissions above rural cells areas due to sink term (about $0.4 - 0.6 \times 10^{15}$ molecules.cm^{-2}.h^{-1} in winter and $0.7 - 0.9 \times 10^{15}$ molecules.cm^{-2}.h^{-1} in summer). It is also observed that TROPOMI NO_2 column densities above this zone are relatively homogeneous, which indicates that the high value for the transport term is due to abrupt changes in wind direction, which is consistent with the presence of the coast. Consequently, a poor representation of the wind field by ERA5, caused by the $0.25° \times 0.25°$ spatial resolution of the data (i.e. about 26 km in this region, the same order of magnitude as the width of the channel) might misestimate the transport term.

4.3 Vertical analysis

Here we investigate the influence of the choice of the vertical level in the representation of the model parameters. This influence is of considerable importance, as NO_x sources in urban areas can be located at different altitudes. For instance, emissions from the road sector from tailpipes are located at ground level, whereas NO_x from power plants and industrial facilities can be emitted from stacks, which are usually located between 50 and 300 m above the ground. The results of Section 4.1 showed that level $\mathcal{B}$ was more appropriate for the representation of the NO_2 lifetime. This level is therefore chosen as a reference for the comparison. We study the effect of a transition from level $\mathcal{B}$ to level $\mathcal{A}$ for each of the 3 parameters involved in the representation of the sink term, i.e. temperature T, hydroxyl radical concentration [OH] and concentration ratio $[NO_x]/[NO_2]$. The results for the averages over urban and rural areas are given for the months of January, April, July and October 2019 in Table 2. As the wind field is only involved in the transport term whose spatial integration nearly leads to zero, the influence of this parameter is not studied.

TITLE		**Sink term (10^{15} molecules.cm^{-2}.h^{-1})**							
level $\mathcal{B}$ (987.5 hPa)	**level $\mathcal{A}$ (925 hPa)**	Jan. 19 (urban)	Jan. 19 (rural)	Apr. 19 (urban)	Apr. 19 (rural)	Jul. 19 (urban)	Jul. 19 (rural)	Oct. 19 (urban)	Oct. 19 (rural)
T, [OH], $\frac{[NO_x]}{[NO_2]}$	-	1.289	0.493	1.737	0.694	1.969	0.788	1.627	0.672
[OH], $\frac{[NO_x]}{[NO_2]}$	T	1.349 (+4.7%)	0.513 (+4.2%)	1.827 (+5.2%)	0.727 (+4.8%)	2.073 (+5.3%)	0.826 (+4.9%)	1.709 (+5.0%)	0.704 (+4.7%)
T, $\frac{[NO_x]}{[NO_2]}$	[OH]	0.968 (-24.9%)	0.366 (-25.7%)	1.504 (-13.4%)	0.603 (-13.1%)	1.837 (-6.7%)	0.750 (-4.8%)	1.403 (-13.8%)	0.573 (-14.7%)
T, [OH]	$\frac{[NO_x]}{[NO_2]}$	1.310 (+1.7%)	0.499 (+1.4%)	1.776 (+2.2%)	0.712 (+2.5%)	1.999 (+1.5%)	0.803 (+1.9%)	1.659 (+2.0%)	0.693 (+3.1%)

Table 2: Analysis of the effect of a vertical change in the parameters used to estimate the sink term in NO_x emissions: temperature, hydroxyl radical concentration, and NO_x:NO_2 concentration ratio. The comparison is conducted between the estimated quantities for level $\mathcal{B}$ and level $\mathcal{A}$. The comparison is conducted for four months of the year 2019. Values within brackets represent the variation from the base case for which all quantities are estimated at level $\mathcal{B}$.

The transition to the level $\mathcal{A}$ generally results in a decrease in temperature, leading to an increase in the reaction rate k_{mean} and thus an increase in the emissions from the sink term. This transition has only a small influence on the total NO_x emission estimates, with the total increasing by 4 to 6%. The effect is slightly more pronounced in urban areas, due to a steeper vertical temperature profile in these areas. The influence of OH goes in the opposite direction: its concentration decreases strongly with altitude, weakening the sink term. The share of emissions due to the sink term being proportional to this parameter, the effect of the vertical is very pronounced. Thus, the transition to level $\mathcal{A}$ weakens the sink term by 4 to 9% in summer (with an average of -6.03% for the months June/July/August) and by 9 to 26% in winter (with an average of -15.70% for the months December/January/February). This weakening seems more pronounced over urban areas than over rural areas from March to October, and more pronounced over rural areas than over urban areas during the rest of the year. Finally, the influence of the NO_x:NO_2 ratio is negligible on the NO_x emission estimates. Thus, the transition to level $\mathcal{A}$ results in an increase in the sink term of 2 to 4%, due to a decrease in both concentrations of NO and NO_2 with respect to the vertical but with a greater decrease for NO_2. This vertical study confirms the crucial importance of the OH concentration representation for the accurate representation of NO_x emissions. OH concentration appears here as the crucial driver of the sink term, much more sensitive to vertical differences than temperature or the NO_x:NO_2 concentration ratio.

4.4 Weekly cycle

In Egypt, the official rest day is Friday, and the economic activity of the country is *a priori* lower during this day than

https://doi.org/10.5194/acp-2021-1051
Preprint. Discussion started: 10 January 2022

Atmospheric Chemistry and Physics Discussions

during the other days of the week. We therefore try to characterise this feature, by evaluating the weekly cycle of NO_x emissions. We use the TROPOMI-inferred emissions to obtain averages per day of the week. We use the quality assurance q_a of TROPOMI retrievals to ignore the days for which more than 20% of the domain has low-quality data (this happens 43 times in 2018/2019 and 28 times in 2019/2020). Figure 8 shows the resulting emissions for the period November 2018 - November 2019 and November 2019 - November 2020. A Friday minimum is observed, defining a marked weekly cycle. This trend is also observed for mean NO_2 column densities, for which no intra-weekly variation is observed. Over the 2018-2019 period, Fridays have average emissions of 0.978 ± 0.408 kt, which is lower than average emissions for the rest of the week, which reach 1.279 ± 0.533 kt. A similar trend is observed in 2019-2020, for which the average for Fridays is 0.856 ± 0.357 kt and the average for other days is 1.067 ± 0.449 kt. The difference in emissions between the two periods is due to smaller emissions in December 2019, January 2020 and February 2020 that are discussed in Section 4.5. On average, Friday emissions correspond to a ratio of 0.81:7 (i.e. a value of 0.81 after normalisation on the seven days of the week) for the entire domain. This result is consistent with the values obtained by Stavrakou et al., 2020 [58], who used TROPOMI data and another emission model to calculate a ratio of 0.71:7 for Cairo and 0.89:7 for Alexandria in 2017.

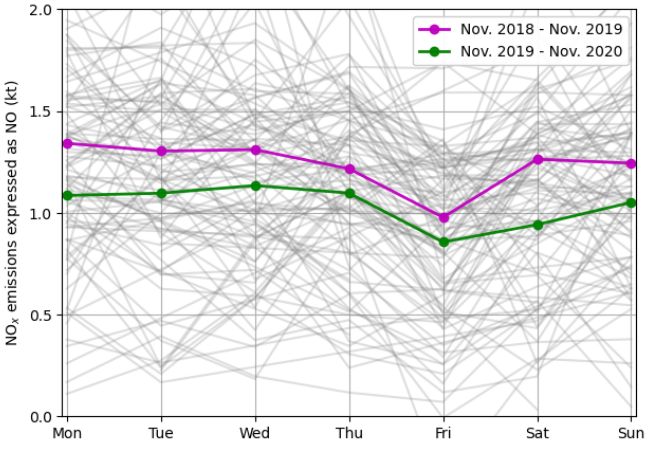

Figure 8: Weekly profiles of anthropogenic NO_x emissions for Egypt using TROPOMI observations in 2018-2019 (purple line) and 2019-2020 (green line). Thin grey lines represent individual weeks. Days for which less than 80% of the domain counts low quality observations ($q_a < 0.75$) are not represented.

4.5 Impacts of lockdown during COVID-19

The ongoing global outbreak of COVID-19 forced many countries around the world to implement unprecedented public health responses, including travel restrictions, quarantines, curfews and lockdowns. Such measures have helped to counter the spread of the virus and have, meanwhile, caused high reductions in global demand for fossil fuels (IEA, 2020 [59]). They also led to a fall in the levels of NO_2 and other air pollutants across the globe (Venter et al., 2020 [60]; Bauwens et al., 2020 [61]; Barré et al., 2021 [62]). To prevent the spread of COVID-19, Egyptian authorities ordered a partial lockdown from March 15th till June 30th 2020, closing all public areas (e.g. sport centres, nightclubs, restaurants and cafes) and suspending religious activities in all mosques and churches throughout the country. They also implemented more drastic measures such as a full lockdown during Easter (April 20th) and Eid (May 23rd to May 25th), resulting in before lifting some restrictions on June 1st (Hale et al., 2021 [63]). In addition to the effect of containment on the activity of the country, the global decline in consumption led to a drop in the production of certain industrial products.

Several studies have estimated the impact of these events on the air pollution levels in the urban centres of the country : from in-situ measurements, El-Sheekh et al., 2021 [64] estimated that NO_2 concentrations had dropped by 25.9% in Alexandria's city centre after the start of the lockdown on March 13th, while El-Magd et al., 2020 [65] used OMI retrievals to estimate a 45.5% reduction of NO_2 concentrations for the entire country during the spring compared to 2018 and 2019 average values. However, due to a changing lifetime of NO_2, reductions in the concentrations of NO_2 might not be entirely due to a drop of NO_x emissions, which leads us to focus on the variation of NO_x emissions during this singular period. Using our top-down emission model, reductions in total NO_x emissions of 34.6%, 17.4%

https://doi.org/10.5194/acp-2021-1051
Preprint. Discussion started: 10 January 2022

Atmospheric Chemistry and Physics Discussions

and 16.6% are observed for the respective months of March, April and May 2020 compared to the equivalent months in 2019. This drop of emissions in 2020 compared to 2019 calculated by the model also correspond to a decrease in observed NO_2 columns. However, no significant changes in OH concentrations seem to appear: on average, from 2019 to 2020, CAMS near-real-time data shows a decrease of 5.5% for OH concentration over the urban cells for the period March/April/May, while TROPOMI retrievals above urban areas show a decrease in NO_2 column densities of 21.6% over the same period. However, these effects observed for the months of March, April and May 2020 are not repeated in June 2020, for which emissions show an increase of 12.3% compared to June 2019. This increase is largely the result of an increase in the difference between urban and rural average emissions (as calculated according to Equation 7). Indeed, the urban term of June 2020 is higher than that of June 2019, due to an increase in TROPOMI urban concentrations (+2.4%) while the NO_2 lifetime is almost unchanged (+0.4%). The rural term varies in the opposite direction: a decrease in TROPOMI rural concentrations (-7.6%) is observed while NO_2 lifetime increases strongly (+11.5%). This increase in June emissions seems to indicate that the lift on restrictions allowed a catch-up of the economic activity which has be sufficiently strong to generate higher emissions in 2020 than in 2019.

4.6 Annual cycle and comparison to inventories

Here, we attempt to compare our TROPOMI-derived NO_x emissions to emissions from CAMS and EDGAR inventories. Figure 9 shows the total anthropogenic NO_x emissions over the urban cells from November 2018 to November 2020 (i.e. a period of two years), with the average anthropogenic emissions calculated according to Equation (7). As indicated in Section 3.2, the emissions, calculated at 13:30 local time, are representative of the average daily consumption in Egypt. The total calculated for each month therefore corresponds to the NO_x production by human activities in Egyptian urban and industrial areas. After aggregating the different sectors of activity, CAMS and EDGAR inventories directly provide the anthropogenic NO_x emissions over the same areas. All NO_x emissions are expressed in mass terms as NO. We note that the EDGAR inventory does not cover the period 2018-2020 (the inventory ends in 2015). On Figure 9, EDGAR emissions corresponding to the period between November 2013 and November 2015 are displayed, i.e. with a delay of 5 years compared to TROPOMI-derived emissions and CAMS estimates. TROPOMI-derived emissions are lower than the inventory estimates between November 2019 and February 2020. In particular, the difference is significant in December 2019 and January 2020 (respectively 54.8% and 55.7% of CAMS levels). In the computations, this decrease is mainly due to a relatively low value of the OH concentration which reaches 5.86 $\times 10^6$ molecules.cm^{-3} on average for these two months, with 4.95 $\times 10^6$ molecules.cm^{-3} above urban areas and 6.09 $\times 10^6$ molecules.cm^{-3} over rural areas. They were respectively 6.96, 6.94 and 6.97 $\times 10^6$ molecules.cm^{-3} for the previous year (December 2018-January 2019) and 7.24, 6.94 and 7.31 $\times 10^6$ molecules.cm^{-3} for the year before (December 2017-January 2018). A decrease in tropospheric columns (-14.3% for urban areas and -4.6% for rural areas) also contributes to this drop.

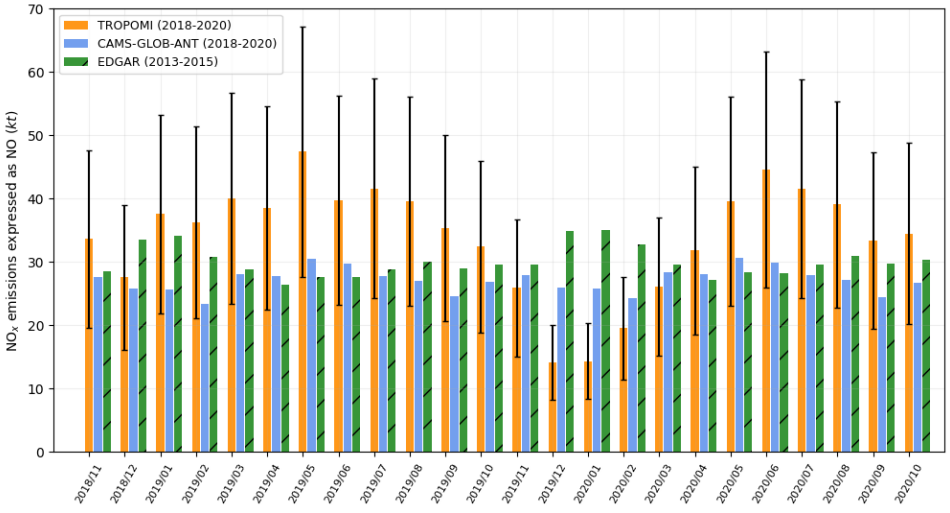

Figure 9: Comparison of TROPOMI-derived NO_x emissions for urban areas in Egypt (light blue), with the corresponding emissions from EDGAR (red with stripes) and CAMS (yellow) inventories. EDGAR data is provided for comparison purposes and covers the years 2013-2015. Error bars for TROPOMI-derived emissions are calculated using uncertainties for the parameters involved in Equation (3).

https://doi.org/10.5194/acp-2021-1051
Preprint. Discussion started: 10 January 2022

Atmospheric Chemistry and Physics Discussions

Except for this singular period, TROPOMI-derived indications of emissions are higher than the CAMS inventory estimates. The top-down model estimates total emissions of 814.5 kt over the 24 months, which is 162.9 kt higher than CAMS for the same period (651.6 kt). Of these 162.9 kt, 125.2 kt are emitted during the first 12 months (before the underestimation period) and 37.7 kt during the 12 following months. The average value for top-down NO_x emissions are 25.0% higher than CAMS estimates. TROPOMI-inferred emissions show an annual variability: the emissions seem to follow a one-year seasonal cycle where emissions are higher in summer than in winter. These results, at first sight, seem to be correlated with power emissions which dominate the use of fossil fuels in Egypt (Abdallah et al., 2020 [66]). These power emissions are due to the country's residential electricity consumption (Attia et al., 2012 [49]; Elharidi et al., 2013 [67]; Nassief, 2014 [68]). They also meet the needs of industry. Summer peaks in electricity consumption are mostly driven by temperature: for instance, the sales of air conditioning and ventilation systems have been increasing for several decades (Wahba et al., 2018 [69]). The use of air conditioning in cars, which requires an additional amount of fuel, could also contribute to the increase of NO_x emissions in summer. However, some features of the industrial activities in the region might be counteracting this trend. For some sectors such as cement or steel, production is lower in summer, due to the physical wear experienced by workers due to heat, but also due to certain periods of leave. Given the importance of industrial activities in the production of NO_x shown in Section 4.2, this aspect cannot be neglected. The transport sector could also counteract the observed trend: although the use of air conditioning in cars increase NO_x emissions of the sector, the observed mean traffic in the country is higher between November and February and lower between June and August, especially in Cairo which gathers most of the population. In the absence of additional data, it therefore seems difficult to conclude on the relevance of the seasonal cycle that seems to be produced by our top-down model. This caution is all the more necessary as CAMS and EDGAR inventories show different seasonal cycles in NO_x emissions, with different dynamics: while the EDGAR inventory predicts a maximum of emissions in December or January and a minimum in April, the CAMS inventory shows two local maxima each year in May and November and two local minima in February and September. The amplitude of the cycle is higher in EDGAR than in CAMS, representing 14.2% of the average value for emissions estimates in EDGAR and 12.4% in CAMS. These differences between the model and the inventories do not give us any information on the seasonality of NO_x emissions that should be found in the outputs of our top-down model.

4.7 Uncertainties and assessments of the previous results

The estimation of NO_x emissions is based on the use of several quantities with varying uncertainties. The error bars shown in Figures 5 and 9 are thus calculated from uncertainty statistics whose references are presented in this section. Since these references do not specify the exact nature of these statistics, we assume they correspond to standard deviations. The uncertainty of tropospheric NO_2 columns under polluted conditions is dominated by the sensitivity of satellite observations to lower tropospheric air masses, expressed by the tropospheric air-mass factor (AMF). The AMF depends on the viewing geometry, surface albedo, NO_2 vertical profile, and cloud characteristics (Lorente et al., 2017 [38]; Eskes et al., 2019 [18]). The column relative uncertainty due to the AMF is of the order of 30% (Boersma et al., 2004 [37]). S-5P validation activities indicate that TROPOMI tropospheric NO_2 columns are systematically biased low by about 30%-50% over cities, which is most likely related to the *a priori* profiles used within the operational retrieval that do not reflect well the NO_2 peak close to ground. For the Middle East region, the impact of the *a priori* profile is less critical, as surface albedo is generally high and cloud fractions are generally low. Thus, we expect no such bias, and consider a relative uncertainty of 30% for the tropospheric column. Other uncertainties must be taken into account: the transition from NO_2 TROPOMI columns to NO_x emissions requires parameters which appear in Equation (2) and Equation (3). For both zonal and meridional wind components, we assume an uncertainty of 1 m/s (Coburn et al., 2019 [70]). For [OH], the analysis of different methods conducted by Huijnen et al., 2019 [71] showed smaller differences for low latitudes than for extratropics, but still significant. We thus take a relative uncertainty of 30% for OH concentration. For the reaction rate k_{mean}, the value of the corresponding relative uncertainty has been estimated by Burkholder et al., 2020 [28]. Because the sensitivity test conducted in Section 4.3 shows that changing the temperature vertically only changes the results by 2-3%, and because vertical temperature gradients are much stronger than horizontal temperature gradients, then the uncertainty related to the horizontal temperature field is small. Therefore, we neglect the impact of temperature on final uncertainty. As a consequence, the propagation of these different uncertainties on the monthly estimates of NO_x emissions in Egypt leads to an expanded uncertainty between 40 and 43%. For lifetimes calculated with the EMG function fitting, the corresponding expanded uncertainty ranges between 18% and 79%.

We acknowledge the fact that our treatment of uncertainties is simplified there. Many minor sinks highlighted in Section 3.1 are neglected in the calculations, and the corresponding uncertainty are not taken into account. Moreover, among the remaining sources of uncertainties, the major ones are treated with fixed values for relative uncertainties,

https://doi.org/10.5194/acp-2021-1051
Preprint. Discussion started: 10 January 2022

which leads to absolute uncertainties that are roughly proportional to monthly emissions. As a result, the confidence interval displayed on Figure 9 is larger in summer than in winter (with a length of 6.0 kt in January 2020 and of 17.4 kt for July 2020), and the drop in emissions for winter 2019-2020 appears as a persistent feature of the model outputs. If this drop is realistic, then our top-down model provides a method for improving national inventories. If it is not, then several assumptions of our model can be questioned. For instance, because this drop is largely due to variations in OH concentrations provided by CAMS, whose reliability has been evaluated for Riyadh, then the transposability hypothesis between Riyadh and Egypt may be subject to wider discussion. A better understanding of OH levels in Egypt, supported by in-situ measurements, might answer these questions and allow to improve our model.

5 Conclusions

In this study, we investigated the potential of a top-down model of NO_x emissions based on TROPOMI retrievals at high resolution over Egypt. The model is based on the study of a transport term and a sink term that requires different parameters to be calculated. Among those parameters, the concentration in OH, involved in the calculation of the NO_2 mixed lifetime, is of fundamental importance. The comparison between the two ways of calculating the lifetime of NO_2 shows that OH concentration provided by CAMS data is reasonably reliable for the country. Parameters are therefore taken in the first 200 m of the planetary boundary layer, because it is where OH shows the best consistency. However, the vertical sensitivity linked to this parameters remains high. Results illustrate the importance of the transport term at local scale, which is the same order of magnitude as the sink term above large cities and industrial facilities; it ceases to be relevant only at the country's scale. The top-down model is able to characterise declines in human activities, whether they are due to restrictions during the COVID-19 pandemic or to Friday rest. It also estimates higher emissions during summer. These high emissions might be interpreted by a higher consumption of electricity driven by air-conditioning during hot days, but it remains unclear whether this pattern clearly reproduces changes in human activity, in particular because the different emission inventories show different seasonalities. These inventories also differ in the amount of total emissions: the average value for TROPOMI-derived NO_x emissions are 25.0% higher than CAMS estimates. This discrepancy could be solved comparing the results of the model and inventory estimates to industrial production or electricity consumption data at the scale of countries or regions. This study demonstrates the potential of TROPOMI data for evaluating NO_x emissions in the EMME region. More generally, it demonstrates the importance of the contribution of independent observation systems to overcome the weaknesses of emission inventories, provided that the local chemistry is well understood. The development of similar applications for different species is likely to allow better monitoring of global anthropogenic emissions, therefore helping companies and countries to report their anthropogenic emissions of air pollutants and greenhouse gases as part of their strategies to tackle air pollution issues and climate change.

Data availability.
CAMS NRT: https://ads.atmosphere.copernicus.eu/cdsapp!/dataset/cams-global-atmospheric-composition-forecasts
ERA5 reanalysis: https://cds.climate.copernicus.eu/cdsapp!/dataset/reanalysis-era5-pressure-levels-monthly-means
Global Rural-Urban Mapping Project (GRUMP): https://sedac.ciesin.columbia.edu/data/collection/grump-v1
Oil and gas power plants: http://globalenergyobservatory.org/
Industrial facilities: https://www.industryabout.com
Flaring sites: https://eogdata.mines.edu/download_global_flare.html
CAMS-GLOB-ANT_v4.2: https://permalink.aeris-data.fr/CAMS-GLOB-ANT
EDGARv5.0: https://edgar.jrc.ec.europa.eu/dataset_ap50

Competing interests. The authors declare that they have no conflict of interest.

Acknowledgements. The authors would like to thank Steven J. Davis (University of California, Irvine) and Dan Tong (Tsinghua University) for their contribution to the construction of our emitters database.

Financial support. This study has been funded by the European Union's Horizon 2020 research and innovation programme under grant agreement N° 856612 (EMME-CARE).

https://doi.org/10.5194/acp-2021-1051
Preprint. Discussion started: 10 January 2022

Atmospheric Chemistry and Physics Discussions

References

[1] A. Baklanov, L. T. Molina, and M. Gauss, "Megacities, air quality and climate," *Atmospheric Environment*, vol. 126, pp. 235–249, 2016.

[2] A. Singh and M. Agrawal, "Acid rain and its ecological consequences," *Journal of Environmental Biology*, vol. 29, no. 1, p. 15, 2007.

[3] U. EPA, "Integrated science assessment for oxides of nitrogen–health criteria," *US Environmental Protection Agency, Washington, DC [Google Scholar]*, 2016.

[4] M. Crippa, G. Janssens-Maenhout, F. Dentener, D. Guizzardi, K. Sindelarova, M. Muntean, R. Van Dingenen, and C. Granier, "Forty years of improvements in European air quality: regional policy-industry interactions with global impacts," *Atmospheric Chemistry and Physics*, vol. 16, no. 6, pp. 3825–3841, 2016.

[5] A. El-Magd, N. Zanaty, E. M. Ali, H. Irie, A. I. Abdelkader, *et al.*, "Investigation of aerosol climatology, optical characteristics and variability over Egypt based on satellite observations and in-situ measurements," *Atmosphere*, vol. 11, no. 7, p. 714, 2020.

[6] UNEP (United Nations Environment Programme), "Air quality policies in Egypt," 2015.

[7] B. Xue and W. Ren, "China's uncertain CO2 emissions," *Nature Climate Change*, vol. 2, no. 11, pp. 762–762, 2012.

[8] C. Leue, M. Wenig, T. Wagner, O. Klimm, U. Platt, and B. Jähne, "Quantitative analysis of NOx emissions from global ozone Monitoring Experiment satellite image sequences," *Journal of Geophysical Research: Atmospheres*, vol. 106, no. D6, pp. 5493–5505, 2001.

[9] R. V. Martin, D. J. Jacob, K. Chance, T. P. Kurosu, P. I. Palmer, and M. J. Evans, "Global inventory of nitrogen oxide emissions constrained by space-based observations of NO2 columns," *Journal of Geophysical Research: Atmospheres*, vol. 108, no. D17, 2003.

[10] B. Mijling and R. Van Der A, "Using daily satellite observations to estimate emissions of short-lived air pollutants on a mesoscopic scale," *Journal of Geophysical Research: Atmospheres*, vol. 117, no. D17, 2012.

[11] B. de Foy, Z. Lu, D. G. Streets, L. N. Lamsal, and B. N. Duncan, "Estimates of power plant NOx emissions and lifetimes from OMI NO2 satellite retrievals," *Atmospheric Environment*, vol. 116, pp. 1–11, 2015.

[12] D. L. Goldberg, Z. Lu, D. G. Streets, B. de Foy, D. Griffin, C. A. McLinden, L. N. Lamsal, N. A. Krotkov, and H. Eskes, "Enhanced Capabilities of TROPOMI NO2: Estimating NOx from North American Cities and Power Plants," *Environmental science & technology*, vol. 53, no. 21, pp. 12594–12601, 2019.

[13] S. Beirle, C. Borger, S. Dörner, A. Li, Z. Hu, F. Liu, Y. Wang, and T. Wagner, "Pinpointing nitrogen oxide emissions from space," *Science advances*, vol. 5, no. 11, p. eaax9800, 2019.

[14] A. Lorente, K. Boersma, H. Eskes, J. Veefkind, J. Van Geffen, M. De Zeeuw, H. D. van der Gon, S. Beirle, and M. Krol, "Quantification of nitrogen oxides emissions from build-up of pollution over Paris with TROPOMI," *Scientific reports*, vol. 9, no. 1, pp. 1–10, 2019.

[15] K. Lange, A. Richter, and J. P. Burrows, "Variability of nitrogen oxide emission fluxes and lifetimes estimated from Sentinel-5P TROPOMI observations," *Atmospheric Chemistry and Physics Discussions*, pp. 1–32, 2021.

[16] J. Veefkind, I. Aben, K. McMullan, H. Förster, J. De Vries, G. Otter, J. Claas, H. Eskes, J. De Haan, Q. Kleipool, *et al.*, "TROPOMI on the ESA Sentinel-5 Precursor: A GMES mission for global observations of the atmospheric composition for climate, air quality and ozone layer applications," *Remote sensing of environment*, vol. 120, pp. 70–83, 2012.

[17] S. Lama, S. Houweling, K. F. Boersma, H. Eskes, I. Aben, H. A. Denier van der Gon, M. C. Krol, H. Dolman, T. Borsdorff, and A. Lorente, "Quantifying burning efficiency in megacities using the NO2/CO ratio from the Tropospheric Monitoring Instrument (TROPOMI)," *Atmospheric Chemistry and Physics*, vol. 20, no. 17, pp. 10295–10310, 2020.

https://doi.org/10.5194/acp-2021-1051
Preprint. Discussion started: 10 January 2022

Atmospheric Chemistry and Physics Discussions

[18] H. Eskes, K. Eichmann, J. Lambert, D. Loyola, J. Veefkind, A. Dehn, and C. Zehner, "S5P Mission Performance Centre Nitrogen Dioxide [l2_no2_] readme," *Royal Netherlands Meteorological Institute (KNMI) De Bilt, the Netherlands, version*, vol. 1, no. 00, 2019.

[19] H. Hersbach, B. Bell, P. Berrisford, S. Hirahara, A. Horányi, J. Muñoz-Sabater, J. Nicolas, C. Peubey, R. Radu, D. Schepers, *et al.*, "The ERA5 global reanalysis," *Quarterly Journal of the Royal Meteorological Society*, vol. 146, no. 730, pp. 1999–2049, 2020.

[20] V. Huijnen, H. Eskes, A. Wagner, M. Schulz, Y. Christophe, M. Ramonet, S. Basart, A. Benedictow, A.-M. Blechschmidt, S. Chabrillat, *et al.*, "Validation report of the CAMS near-real-time global atmospheric composition service: System evolution and performance statistics. Status up to 1 June 2016.," 2016.

[21] J. H. Seinfeld, "Urban air pollution: state of the science," *Science*, vol. 243, no. 4892, pp. 745–752, 1989.

[22] J. A. Logan, M. J. Prather, S. C. Wofsy, and M. B. McElroy, "Tropospheric chemistry: a global perspective," *Journal of Geophysical Research: Oceans*, vol. 86, no. C8, pp. 7210–7254, 1981.

[23] H. Levy, "Normal atmosphere: Large radical and formaldehyde concentrations predicted," *Science*, vol. 173, no. 3992, pp. 141–143, 1971.

[24] L. Valin, A. Russell, R. Hudman, and R. Cohen, "Effects of model resolution on the interpretation of satellite NO2 observations," *Atmospheric Chemistry and Physics*, vol. 11, no. 22, pp. 11647–11655, 2011.

[25] J. Lelieveld, S. Gromov, A. Pozzer, and D. Taraborrelli, "Global tropospheric hydroxyl distribution, budget and reactivity," *Atmospheric Chemistry and Physics*, vol. 16, no. 19, pp. 12477–12493, 2016.

[26] M. Li, E. Karu, C. Brenninkmeijer, H. Fischer, J. Lelieveld, and J. Williams, "Tropospheric OH and stratospheric OH and Cl concentrations determined from CH4, CH3Cl, and SF6 measurements," *NPJ Climate and Atmospheric Science*, vol. 1, no. 1, pp. 1–7, 2018.

[27] G. M. Wolfe, J. M. Nicely, J. M. S. Clair, T. F. Hanisco, J. Liao, L. D. Oman, W. B. Brune, D. Miller, A. Thames, G. G. Abad, *et al.*, "Mapping hydroxyl variability throughout the global remote troposphere via synthesis of airborne and satellite formaldehyde observations," *Proceedings of the National Academy of Sciences*, vol. 116, no. 23, pp. 11171–11180, 2019.

[28] J. Burkholder, S. Sander, J. Abbatt, J. Barker, C. Cappa, J. Crounse, T. Dibble, R. Huie, C. Kolb, M. Kurylo, *et al.*, "Chemical kinetics and photochemical data for use in atmospheric studies; evaluation number 19," tech. rep., Pasadena, CA: Jet Propulsion Laboratory, National Aeronautics and Space . . . , 2020.

[29] K. Boersma, H. Eskes, E. Meijer, and H. Kelder, "Estimates of lightning NOx production from gome satellite observations," *Atmospheric Chemistry and Physics*, vol. 5, no. 9, pp. 2311–2331, 2005.

[30] J. Yienger and H. Levy, "Empirical model of global soil-biogenic NOx emissions," *Journal of Geophysical Research: Atmospheres*, vol. 100, no. D6, pp. 11447–11464, 1995.

[31] CIESIN, "CIESIN. Global Rural-Urban Mapping Project, Version 1 (GRUMPv1). Center for International Earth Science Information Network - CIESIN - Columbia University, International Food Policy Research Institute - IFPRI, The World Bank, and Centro Internacional de Agricultura Tropical - CIAT. 2011, Palisades, NY: NASA Socioeconomic Data and Applications Center (SEDAC)," 2019.

[32] C. D. Elvidge, M. Zhizhin, K. Baugh, F.-C. Hsu, and T. Ghosh, "Methods for global survey of natural gas flaring from visible infrared imaging radiometer suite data," *Energies*, vol. 9, no. 1, p. 14, 2016.

[33] M. Crippa, G. Oreggioni, D. Guizzardi, M. Muntean, E. Schaaf, E. Lo Vullo, E. Solazzo, F. Monforti-Ferrario, J. G. Olivier, and E. Vignati, "Fossil CO2 and GHG emissions of all world countries," *Publication Office of the European Union: Luxemburg*, 2019.

[34] C. Granier, S. Darras, H. D. van der Gon, D. Jana, N. Elguindi, G. Bo, G. Michael, G. Marc, J.-P. Jalkanen, J. Kuenen, *et al.*, *The Copernicus atmosphere monitoring service global and regional emissions (April 2019 version)*. PhD thesis, Copernicus Atmosphere Monitoring Service, 2019.

https://doi.org/10.5194/acp-2021-1051
Preprint. Discussion started: 10 January 2022

Atmospheric Chemistry and Physics Discussions

[35] R. M. Hoesly, S. J. Smith, L. Feng, Z. Klimont, G. Janssens-Maenhout, T. Pitkanen, J. J. Seibert, L. Vu, R. J. Andres, R. M. Bolt, *et al.*, "Historical (1750–2014) anthropogenic emissions of reactive gases and aerosols from the community emissions data system (CEDS)," *Geoscientific Model Development*, vol. 11, no. 1, pp. 369–408, 2018.

[36] G. Janssens-Maenhout, M. Crippa, D. Guizzardi, M. Muntean, E. Schaaf, F. Dentener, P. Bergamaschi, V. Pagliari, J. G. Olivier, J. A. Peters, *et al.*, "Edgar v4. 3.2 global atlas of the three major greenhouse gas emissions for the period 1970–2012," *Earth System Science Data*, vol. 11, no. 3, pp. 959–1002, 2019.

[37] K. Boersma, H. Eskes, and E. Brinksma, "Error analysis for tropospheric NO2 retrieval from space," *Journal of Geophysical Research: Atmospheres*, vol. 109, no. D4, 2004.

[38] A. Lorente, K. Folkert Boersma, H. Yu, S. Dörner, A. Hilboll, A. Richter, M. Liu, L. N. Lamsal, M. Barkley, I. D. Smedt, *et al.*, "Structural uncertainty in air mass factor calculation for NO2 and HCHO satellite retrievals," *Atmospheric Measurement Techniques*, vol. 10, no. 3, pp. 759–782, 2017.

[39] S. Sander, R. Friedl, J. Abbatt, J. Barker, J. Burkholder, D. Golden, C. Kolb, M. Kurylo, G. Moortgat, P. Wine, *et al.*, "Chemical kinetics and photochemical data for use in atmospheric studies, jpl publication 10-6," *Evaluation*, no. 17, 2011.

[40] E. R. Delaria, B. K. Place, A. X. Liu, and R. C. Cohen, "Laboratory measurements of stomatal NO2 deposition to native california trees and the role of forests in the NOx cycle," *Atmospheric Chemistry and Physics*, vol. 20, no. 22, pp. 14023–14041, 2020.

[41] N. Sobanski, J. Thieser, J. Schuladen, C. Sauvage, W. Song, J. Williams, J. Lelieveld, and J. N. Crowley, "Day and night-time formation of organic nitrates at a forested mountain site in south-west germany," *Atmospheric Chemistry and Physics*, vol. 17, no. 6, pp. 4115–4130, 2017.

[42] P. S. Romer Present, A. Zare, and R. C. Cohen, "The changing role of organic nitrates in the removal and transport of NOx," *Atmospheric Chemistry and Physics*, vol. 20, no. 1, pp. 267–279, 2020.

[43] N. Butkovskaya, A. Kukui, N. Pouvesle, and G. Le Bras, "Formation of nitric acid in the gas-phase HO2+NO reaction: Effects of temperature and water vapor," *The Journal of Physical Chemistry A*, vol. 109, no. 29, pp. 6509–6520, 2005.

[44] N. Butkovskaya, M.-T. Rayez, J.-C. Rayez, A. Kukui, and G. Le Bras, "Water vapor effect on the HNO3 yield in the HO2+NO reaction: experimental and theoretical evidence," *The Journal of Physical Chemistry A*, vol. 113, no. 42, pp. 11327–11342, 2009.

[45] W. Moxim, H. Levy, and P. Kasibhatla, "Simulated global tropospheric PAN: Its transport and impact on NOx," *Journal of Geophysical Research: Atmospheres*, vol. 101, no. D7, pp. 12621–12638, 1996.

[46] C. A. Longfellow, A. Ravishankara, and D. R. Hanson, "Reactive uptake on hydrocarbon soot: Focus on NO2," *Journal of Geophysical Research: Atmospheres*, vol. 104, no. D11, pp. 13833–13840, 1999.

[47] T. Stavrakou, J.-F. Müller, K. Boersma, R. Van Der A, J. Kurokawa, T. Ohara, and Q. Zhang, "Key chemical NOx sink uncertainties and how they influence top-down emissions of nitrogen oxides," *Atmospheric Chemistry and Physics*, vol. 13, no. 17, pp. 9057–9082, 2013.

[48] N. Friedrich, P. Eger, J. Shenolikar, N. Sobanski, J. Schuladen, D. Dienhart, B. Hottmann, I. Tadic, H. Fischer, M. Martinez, *et al.*, "Reactive nitrogen around the arabian peninsula and in the mediterranean sea during the 2017 AQABA ship campaign," *Atmospheric Chemistry and Physics*, vol. 21, no. 10, pp. 7473–7498, 2021.

[49] S. Attia, A. Evrard, and E. Gratia, "Development of benchmark models for the Egyptian residential buildings sector," *Applied Energy*, vol. 94, pp. 270–284, 2012.

[50] EEHC, "Egyptian Electricity Holding Company annual report 2019/2020," 2021.

[51] F. Rohrer and H. Berresheim, "Strong correlation between levels of tropospheric hydroxyl radicals and solar ultraviolet radiation," *Nature*, vol. 442, no. 7099, pp. 184–187, 2006.

[52] S. Beirle, K. F. Boersma, U. Platt, M. G. Lawrence, and T. Wagner, "Megacity emissions and lifetimes of nitrogen oxides probed from space," *Science*, vol. 333, no. 6050, pp. 1737–1739, 2011.

https://doi.org/10.5194/acp-2021-1051
Preprint. Discussion started: 10 January 2022

Atmospheric Chemistry and Physics Discussions

[53] L. Valin, A. Russell, and R. Cohen, "Variations of OH radical in an urban plume inferred from NO2 column measurements," *Geophysical Research Letters*, vol. 40, no. 9, pp. 1856–1860, 2013.

[54] M. Filioglou, E. Giannakaki, J. Backman, J. Kesti, A. Hirsikko, R. Engelmann, E. O'Connor, J. T. Leskinen, X. Shang, H. Korhonen, *et al.*, "Optical and geometrical aerosol particle properties over the United Arab Emirates," *Atmospheric Chemistry and Physics*, vol. 20, no. 14, pp. 8909–8922, 2020.

[55] T. Graedel, L. Farrow, and T. Weber, "Kinetic studies of the photochemistry of the urban troposphere," *Atmospheric Environment (1967)*, vol. 10, no. 12, pp. 1095–1116, 1976.

[56] J. H. Seinfeld and S. N. Pandis, "Atmospheric chemistry and physics from air pollution to climate change," 2006.

[57] J.-T. Lin, "Satellite constraint for emissions of nitrogen oxides from anthropogenic, lightning and soil sources over East China on a high-resolution grid," *Atmospheric Chemistry and Physics*, vol. 12, no. 6, pp. 2881–2898, 2012.

[58] T. Stavrakou, J.-F. Müller, M. Bauwens, K. Boersma, and J. van Geffen, "Satellite evidence for changes in the NO2 weekly cycle over large cities," *Scientific reports*, vol. 10, no. 1, pp. 1–9, 2020.

[59] U. IEA, "Global energy review 2020," *Ukraine.[Online] https://www. iea. org/countries/ukraine [Accessed: 2020-09-10]*, 2020.

[60] Z. S. Venter, K. Aunan, S. Chowdhury, and J. Lelieveld, "COVID-19 lockdowns cause global air pollution declines," *Proceedings of the National Academy of Sciences*, vol. 117, no. 32, pp. 18984–18990, 2020.

[61] M. Bauwens, S. Compernolle, T. Stavrakou, J.-F. Müller, J. Van Gent, H. Eskes, P. F. Levelt, R. van der A, J. Veefkind, J. Vlietinck, *et al.*, "Impact of coronavirus outbreak on NO2 pollution assessed using TROPOMI and OMI observations," *Geophysical Research Letters*, vol. 47, no. 11, p. e2020GL087978, 2020.

[62] J. Barré, H. Petetin, A. Colette, M. Guevara, V.-H. Peuch, L. Rouil, R. Engelen, A. Inness, J. Flemming, C. Pérez García-Pando, *et al.*, "Estimating lockdown-induced european NO2 changes using satellite and surface observations and air quality models," *Atmospheric Chemistry and Physics*, vol. 21, no. 9, pp. 7373–7394, 2021.

[63] T. Hale, N. Angrist, R. Goldszmidt, B. Kira, A. Petherick, T. Phillips, S. Webster, E. Cameron-Blake, L. Hallas, S. Majumdar, *et al.*, "A global panel database of pandemic policies (oxford covid-19 government response tracker)," *Nature Human Behaviour*, vol. 5, no. 4, pp. 529–538, 2021.

[64] M. M. El-Sheekh and I. A. Hassan, "Lockdowns and reduction of economic activities during the COVID-19 pandemic improved air quality in Alexandria, Egypt," *Environmental Monitoring and Assessment*, vol. 193, no. 1, pp. 1–7, 2021.

[65] I. Abou El-Magd and N. Zanaty, "Impacts of short-term lockdown during COVID-19 on air quality in Egypt," *The Egyptian Journal of Remote Sensing and Space Science*, 2020.

[66] L. Abdallah and T. El-Shennawy, "Evaluation of CO2 emission from Egypt's future power plants," *Euro-Mediterranean Journal for Environmental Integration*, vol. 5, no. 3, pp. 1–8, 2020.

[67] A. M. A. H. Elharidi, P. G. Tuohy, and M. Teamah, "Facing the growing problem of the electric power consumption in Egyptian residential building using building performance simulation program," in *Building simulation Cairo 2013 conference*, 2013.

[68] M. M. Nassief, "Evaluation of electricity consumption of a residential flat in egypt," *American Journal of Electrical Power and Energy Systems*, vol. 3, no. 2, pp. 7–44, 2014.

[69] S. M. Wahba, B. A. Kamel, K. M. Nassar, and A. S. Abdelsalam, "Effectiveness of green roofs and green walls on energy consumption and indoor comfort in arid climates," *Civil Engineering Journal*, vol. 4, no. 10, pp. 2284–2295, 2018.

[70] J. J. Coburn, "Assessing wind data from reanalyses for the upper midwest," *Journal of Applied Meteorology and Climatology*, vol. 58, no. 3, pp. 429–446, 2019.

[71] V. Huijnen, A. Pozzer, J. Arteta, G. Brasseur, I. Bouarar, S. Chabrillat, Y. Christophe, T. Doumbia, J. Flemming, J. Guth, *et al.*, "Quantifying uncertainties due to chemistry modelling–evaluation of tropospheric composition simulations in the CAMS model (cycle 43r1)," *Geoscientific Model Development*, vol. 12, no. 4, pp. 1725–1752, 2019.